Photoacoustic microscopy based on transparent piezoelectric ultrasound transducers

Hangbing Peng*, Zhongwen Cheng*, Lvming Zeng*,†,‡ and Xuanrong Ji*

*State Key Laboratory of Precision Electronics Manufacturing
Technology and Equipment
Guangdong University of Technology
Guangzhou 510006, China

†Key Lab of Optic-Electronic and Communication
Jiangxi Science and Technology Normal University
Nanchang 330038, China
‡zenglvming@163.com

Photoacoustic microscopy (PAM), due to its deep penetration depth and high contrast, is playing an increasingly important role in biomedical imaging. PAM imaging systems equipped with conventional ultrasound transducers have demonstrated excellent imaging performance. However, these opaque ultrasonic transducers bring some constraints to the further development and application of PAM, such as complex optical path, bulky size, and difficult to integrate with other modalities. To overcome these problems, ultrasonic transducers with high optical transparency have appeared. At present, transparent ultrasonic transducers are divided into optical-based and acoustic-based sensors. In this paper, we mainly describe the acoustic-based piezoelectric transparent transducers in detail, of which the research advances in PAM applications are reviewed. In addition, the potential challenges and developments of transparent transducers in PAM are also demonstrated.

Keywords: Photoacoustic microscopy; transparent ultrasound transducer; LiNbO$_3$; PMN-PT; PVDF; CMUT.

1. Introduction

Photoacoustic microscopy (PAM) is a new hybrid imaging modality developed in recent decades, which combines the high contrast of optical imaging with the deep penetration depth of ultrasound imaging. Undoubtedly it has attracted great attention in the field of biomedical imaging applications.[1–3] Based on the specific light absorption of endogenous chromophores (such as hemoglobin), it can be used for single-cell imaging,[4] vasculature imaging,[5–7] and
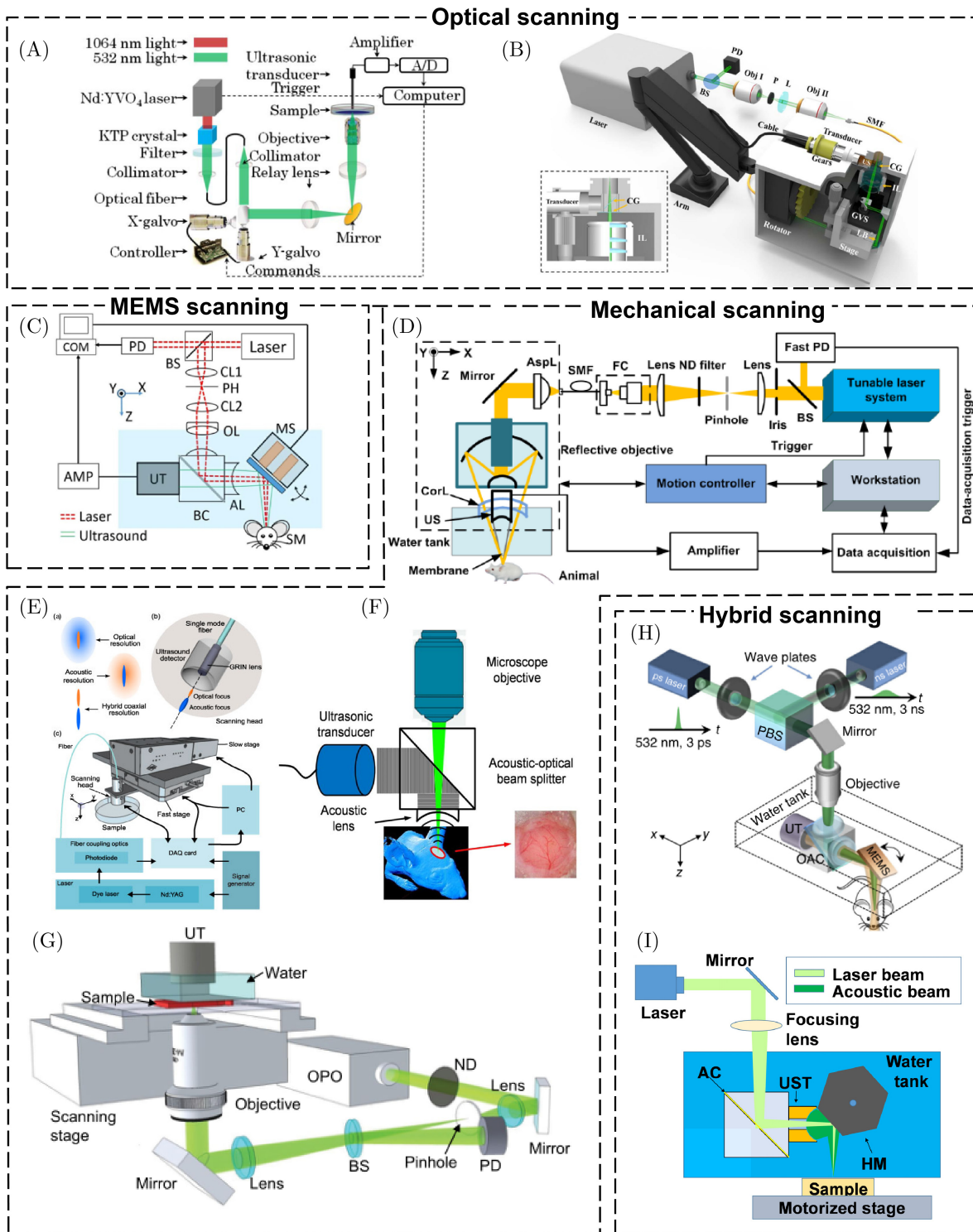
Fig. 1. (A) and (B) Optical scanning of optical beams only. The galvanometer scans the optical beams only. Adapted with permission from Refs. 11 and 12. (C) MEMS scanning of both optical and acoustic beams. All beams are reflected by a two-axis water-immersed MEMS scanner. Adapted with permission from Ref. 13. (D) Mechanical scanning by using dark field illumination. Adapted with permission from Ref. 15. (E) Mechanical scanning by using the ring transducer. Adapted with permission from Ref. 17. (F) Mechanical scanning by using the acoustic-optical beam splitter. Adapted with permission from Ref. 20. (G) PAM with transmission mode. Adapted with permission from Ref. 22. (H) Hybrid scanning by using a one-axis MEMS scanner and a linear stage. Adapted with permission from Ref. 23. (I) Hybrid scanning by using a hexagon-mirror and a linear stage. Adapted with permission from Ref. 24.

imaging of tumors.[8] PAM is characterized by the use of laser beams to excite biological tissues and the employment of the sensors to detect photo-acoustic (PA) signals generated from chromophores in the region of interest (ROI), with lateral resolution ranging from submicrometers to millimeters. Depending on whether the optical or the acoustic foci is tighter, PAM can be classified into optical-resolution PAM (OR-PAM) and acoustic-resolution PAM (AR-PAM).[9]

Conventionally, PAM can be implemented into two major categories: (1) Optical scanning of optical beams only and (2) MEMS scanning or mechanical scanning of both optical and acoustic beams. For the first solution, only optical beams are deflected by the galvanometer scanner to realize fast imaging (Figs. 1(A) and 1(B)).[10–12] Nevertheless, the size of the focal spot or the efficient aperture of the transducer leads to limited imaging field of view (FOV, < 6 mm).[12] The second solution differs from optical scanning, because both the optical and sound beams are scanned confocally through a two-axis MEMS scanner[13,14] (Fig. 1(C)) or a motorized stage (Figs. 1(D)–1(G)). While the two axis MEMS scanner has small geometries and fast imaging speed, a necessary water tank for integrating the scanner and the combiner undoubtedly can increase the system's complexity. Moreover, such a MEMS scanner is both unstable and expensive.[13] By contrast, although mechanical scanning has a relatively slow imaging speed, it can achieve coaxial and confocal alignment of both the optical and acoustic beams more easily. For example, the dark field illumination[15,16] (Fig. 1(D)) enables the PA alignment by deflecting optical beams to bypass the focused ultrasound transducer, but obviously the bending light leads to a dark region in the near field of the transducer, resulting in a long working distance and introducing potential high frequency ultrasonic attenuation. This problem can be overcome either by customized ring transducers (Fig. 1 (E))[17,18] or through PA beam combiners[19–21] (Fig. 1 (F)). Ring transducers allow the light to pass directly through the central aperture of itself at the expense of the reduced sensitivity, while PA beam combiners enable on-axis illumination by complicating the imaging head. Furthermore, the transmission mode (Fig. 1(G))[22] as a simple method to achieve alignment of both the optical and acoustic beams is inappropriate for imaging of thick and optically-scattering biological tissues. Also, several

hybrid scanning methods involving 1D optical scanning and 1D mechanical scanning are proposed in some literatures.[23–25] In this approach, either an one-axis MEMS scanner or hexagon-mirror can fast scan the PA beams along the B-scan direction (Figs. 1(H) and 1(I)), while another direction is scanned by the motor. Although this compromised scanning method can extend the FOV to 12 mm with a high imaging speed, it cannot miniaturize the imaging head due to the motorized linear stage. Overall, all of these implementations have some problems more or less due to the opacity of the transducer. Using transparent sensors can effectively solve the limitations mentioned above in some extents, because the transparency of the sensors allows it a part of both the optical and acoustic path, which can simultaneously realize a fast scanning speed, a large imaging FOV and a simple imaging head. All-optical detectors (such as optical micro ring resonators)[26] with high sensitivity seem to be a good choice, but complex fabrication process of the detectors and bulky imaging systems limit their applications.

Recently, transparent ultrasound transducers (TUTs) have appeared as a new type of sensors which can provide a simple and effective PAM implementation way. Without additional optical components, TUTs can easily achieve PA coaxial and confocal alignment by sharing the optical and acoustic path. In the field of PAM, TUTs have been proved to adapt different imaging occasions in recent years, such as miniaturized and real-time wearable applications. Thus, in Sec. 2 of this review, we mainly introduce the types of TUTs and the research advances in PAM so far. Following this, in Sec. 3, potential challenges and future directions in the development of PAM based on TUTs are demonstrated.

2. PAM based on TUTs

In PAM, PA signals received by the transducer are used to reconstruct the image, so the acoustic performance of the TUT, which is determined by various factors, such as design and manufacturing process can greatly influence the image quality. Concurrently, unlike ordinary nontransparent transducers, all materials that make up the TUT, including the acoustic matching layer, active layer, electrodes and backing layer, need to remain highly transparent in a broad spectrum. According to the

previous reported literature, TUTs can be divided into four types: (1) LiNbO$_3$-based TUTs, (2) PMN-PT-based (lead magnesium niobate-lead titanate) TUTs, (3) PVDF-based (polyvinylidene fluoride) TUTs, and (4) transparent CMUTs, where the last one is accessible to capacitive sensing compared with the first three kinds.

2.1. *PAM based on LiNbO$_3$-TUTs*

Lithium niobate (LiNbO$_3$) is a commonly used piezoelectric single crystal material with high electromechanical coupling efficiency ($Kt \sim 0.5$), high longitudinal sound speed (~ 7340 m/s), and low dielectric constant.[27] On the other hand, LiNbO$_3$ has an optical transmittance greater than 80% in the visible to near-infrared (NIR) spectrum, which is very suitable for fabricating TUTs. The first TUT based on LiNbO$_3$ was made by Graham W. J. Brodie in 2014,[28] in which the author replaced the conventional opaque silver electrodes with the transparent indium-tin oxide (ITO) electrodes. Experiments show that ITO-TUT is similar to silver-transducer in terms of the acoustic performance, such as effective electromechanical coupling coefficient (K_{eff}, 0.44 versus 0.46) and generated sound pressure (loss < 4 dB). Additionally, the optical transmittance of the ITO-TUT is comparable to the uncoated LiNbO$_3$ (< 15% in the 500–800 nm wavelength).

Based on the above progress, Dangi *et al.*[29,30] in 2019 fabricated two TUTs with different geometries for PAM: (1) The first one for endoscopy has a window size of 2.5 mm × 2.5 mm and a long housing filled with nonconductive epoxy as a backing layer for fiber integration (Fig. 2(A)). (2) The second one for microscopy has a larger window size of 10 mm × 10 mm, which is up to four times than the former (Fig. 2(B)). The first TUT suitable for mechanical scanning has a central frequency of 14.2 MHz, a pulse echo bandwidth of 30%, and a transmission rate of more than 80% in the visible and NIR ranges. However, the employment of nonfocused laser beams reduces the lateral resolution of the system, which is only about 900 μm during imaging of the resolution target. Therefore, the system can be improved by adding a fiber coupled graded-index (GRIN) lens for OR-PAM or acoustic lens for AR-PAM. Unlike the first TUT, the advantage of the second window-TUT is that larger window-size allows the laser beams to optically scan samples directly through the transducer,

enabling fast imaging speed and large FOV compatibility. However, the poor signal-to-noise-ratio (SNR, 38 dB in the case of averaging 100 times) becomes the main limitation of the TUT as there is no matching layer for impedance matching or acoustic lens for focusing.

To improve the TUT mentioned above, Liao *et al.*[31] proposed a centimeter-scale window-TUT stacked with a matching layer to further enlarge the FOV and increase the SNR (Fig. 2(C)). The window size of the transducer reaches 2 cm × 2 cm, which is double the size over described earlier, while epoxy matching layer is added and the backing layer is removed to increase the SNR. Figure 2(D) depicts the maximum amplitude projection (MAP) image of the subcutaneous vasculature of the mouse ear and nude abdomen, which fully demonstrates that not only has the system a sufficient lateral resolution (~ 17.5 μm), but also achieves a large enough FOV (18 mm × 18 mm) and SNR. Meanwhile, the use of the galvanometer greatly increases the imaging speed (up to 100 Hz over 1 mm), indicating that the system based on this TUT has great potential to achieve fast subcutaneous micro-vascular imaging of large organs (brain, breast, limbs, etc.). However, system deficiencies still exist, such as the low center frequency (~ 10 MHz) caused by the LiNbO$_3$ crystal's thickness (~ 365 μm) and bandwidth ($\sim 16.46\%$) of the TUT (Fig. 2(C)), which affects the axial resolution and image quality. In this regard, Chen *et al.*[32] developed a higher frequency (37 MHz) window-TUT with up to 90% peak transmittance where the -6 dB bandwidth can reach 33.9%, as shown in Fig. 2(E). The thickness of the LiNbO$_3$ material reached 100 μm. However, the SNR is still limited so that the mouse ear vasculature cannot be resolved clearly (Fig. 2(F)); In terms of bandwidth, Chen *et al.*[33] found that the design of double matching layer (glass and parylene C) can greatly improve the bandwidth of the LiNbO$_3$-TUT by 36% over no matching layer, of which pulse echo bandwidth can reach 51.6% at 14 MHz.

2.2. *PAM based on PMN-PT-TUTs*

Compared to LiNbO$_3$ materials, PMN-PT (lead magnesium niobate-lead titanate) represents a higher piezoelectric constant and better electromechanical coupling properties, which is ideal for low frequency PAM imaging applications.[34] Nevertheless, PMN-PT is generally opaque. To enhance the transparency,
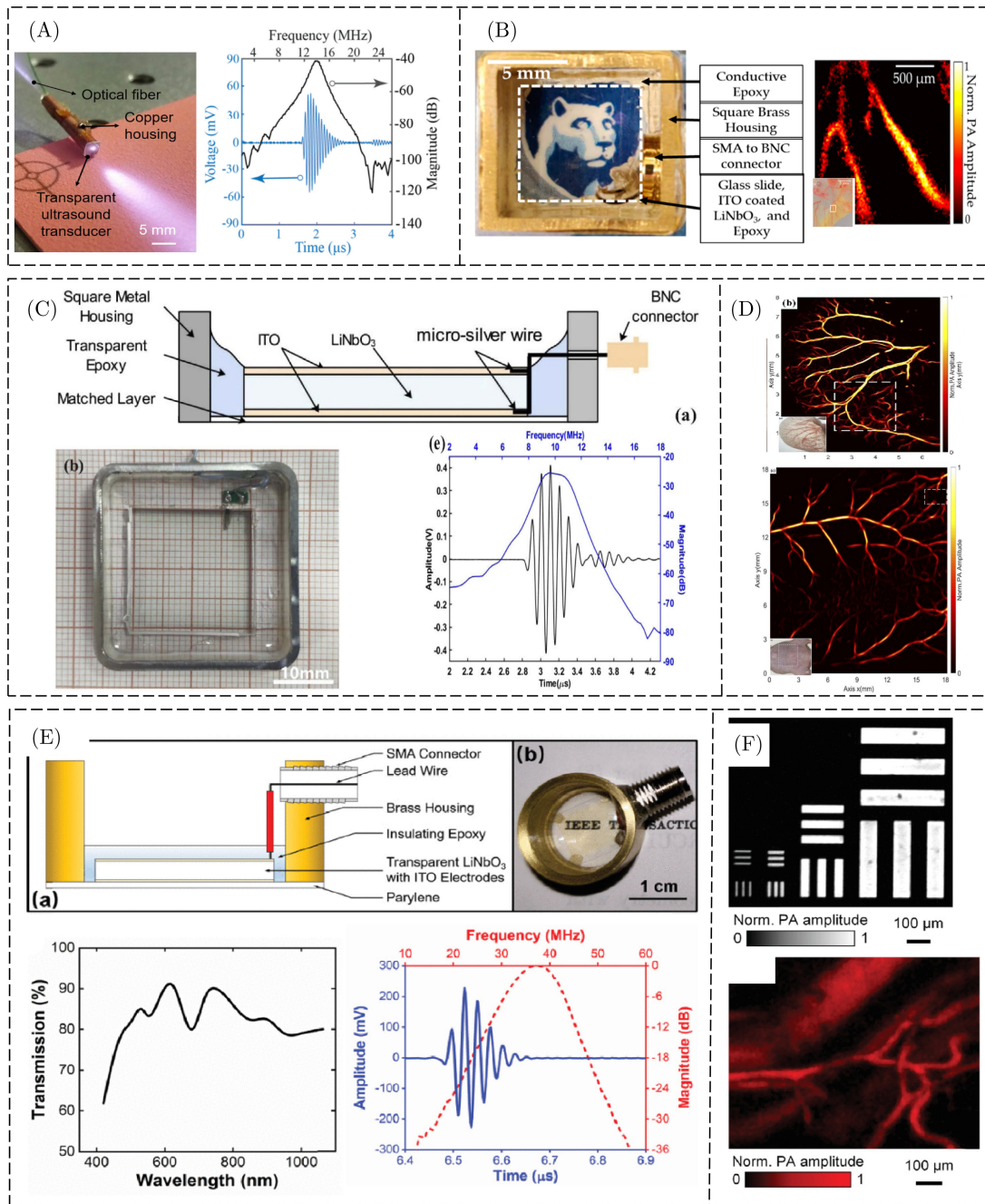
Fig. 2. (A) An optical photo and the time-frequency response of the miniaturized optically transparent 2.5 mm × 2.5 mm transducer integrated with an optical fiber. Adapted with permission from Ref. 29. (B) Schematic cross-sectional view of the 9 mm × 9 mm window-TUT, the photograph and the imaging result of the chicken-embryo membrane. Adapted with permission from Ref. 30. (C) The cross-sectional schematic view, photograph and time-frequency response of the fabricated 33 mm × 33 mm TUT. (D) Photograph and MAP image of the mouse ear and nude mouse abdomen, respectively. Adapted with permission from Ref. 31. (E) Schematic view, photograph, optical transmittance and time-frequency response of the 37 MHz TUT. (F) The MAP image of the resolution target and mouse ear. Adapted with permission from Ref. 32.

Zhang *et al.*[35] fabricated new La-doped lead PMN-PT ceramics with an optical transmittance over 70% (where the light wavelength is 900 nm). Qiu *et al.*[36] reported a high-transparency, high-sensitivity, and ultrahigh-piezoelectricity ($d_{33} > 2100\,pc/N$) PMN-28PT through alternating current (AC) polarization, which further makes it possible for making PMN-PT-based TUTs.
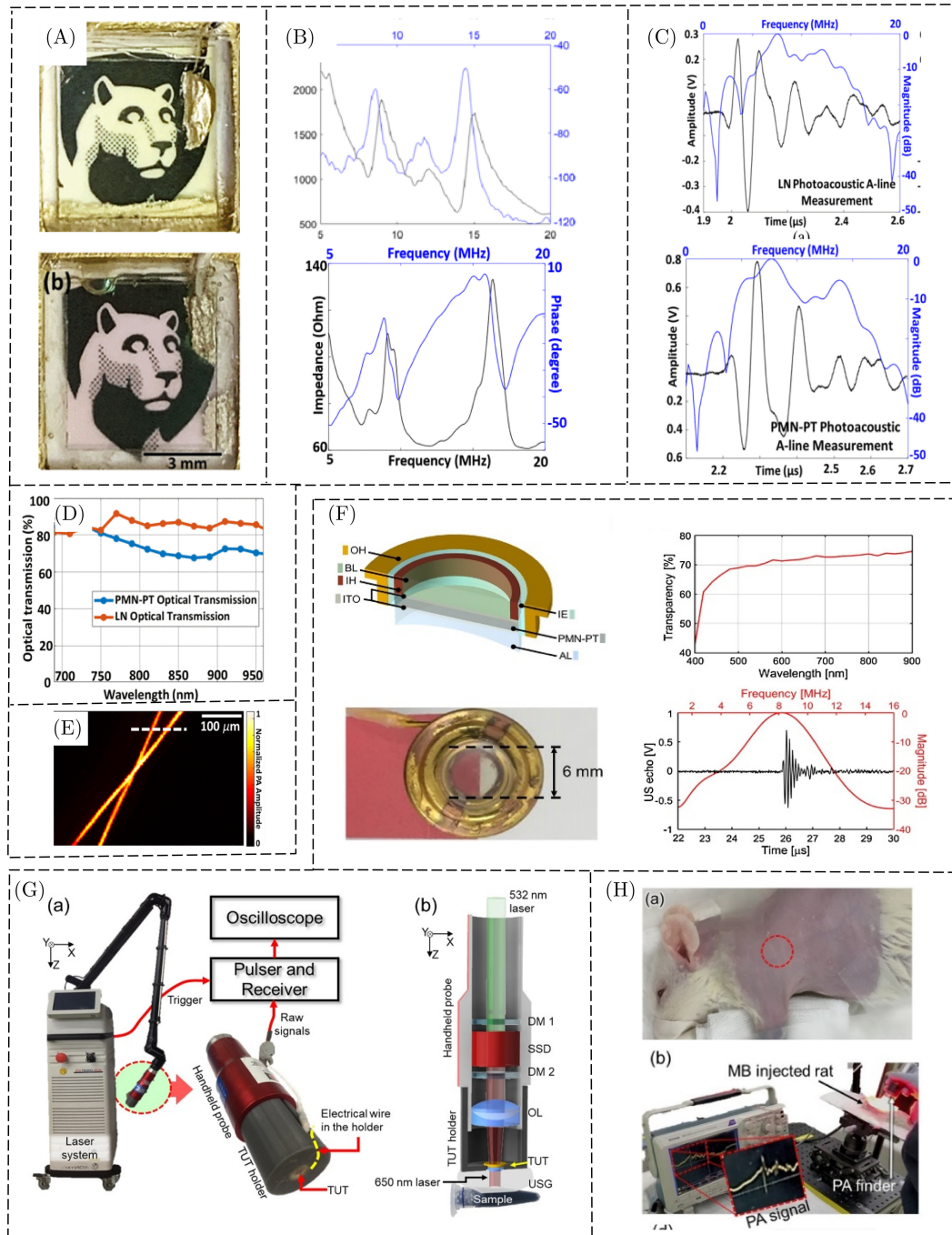
Fig. 3. (A) Picture comparison, (B) impedance-phase plots, (C) PA A-line measurement, and (D) optical transmission plots in near-infrared spectrum of the LiNbO$_3$-TUT (top) and PMN-PT-TUT (bottom). (E) The imaging result of the carbon fibers based on a PMN-PT-TUT. Adapted with permission from Refs. 33 and 37. (F) Layer-by-layer view, photograph, optical transparency, pulse-echo response and spectrum of the TUT. (G) Schematic of the handheld PA finder system and detailed schematic of the handheld probe. (H) Photograph of the rat injected methylene blue and snapshot from the SLN localization experiment video. Adapted with permission from Ref. 38.

Based on progress in materials, Chen *et al.*[33,37] fabricated a PMN-PT-TUT and compared its performance with the LiNbO$_3$-TUT (Fig. 3(A)). The results show that the AC-poled PMN-PT-TUT is superior in terms of electromechanical coupling coefficient (K_{eff}, 0.655 versus 0.376, Fig. 3(B)), PA sensitivity (1.329 V versus 0.678 V, Fig. 3(C)) and SNR (48.9 dB versus 43.7 dB, Fig. 3(C)) due to its

very high piezoelectric constant (2100 pc/N versus 40 pc/N). Also, note that the electrical impedance ($\sim 60\,\Omega$, Fig. 3(B)) of the PMN-PT-TUT is smaller than that of the LiNbO$_3$-TUT ($\sim 500\,\Omega$), indicating that the PMN-PT-TUT are more compatible with back-end amplifier circuits. However, the disadvantage of this type of the TUT lies in lower light transmittance in comparison to LiNbO$_3$-TUT (Fig. 3(D)). Figure 3(E) shows the imaging capability of the OR-PAM using PMN-PT-TUT with the lateral resolution reaching 5 μm; Park *et al.*[38] also developed a low-frequency PMN-PT-TUT for positioning sentinel lymph nodes (SLN) (Fig. 3(F)). The center frequency and transparency of the TUT is 8 MHz, 80% (where the light wavelength is 650 nm), respectively. The sound lens fabricated by epoxy acoustically provides a 19 mm long focal spot for detecting PA signals from deep tissues. In this study, the author combined the TUT with a solid dye laser to create a handheld PAM system (Fig. 3 (G)) for PA A-line detection of mouse SLNs and subcutaneous melanoma. Although the system successfully achieves a live SLN detection in mice (Fig. 3(H)), for humans the blockage of substances such as blood and lipids makes PA signals from SLNs difficult to detect. Thus, further improvements for the system are needed such as the development of lower frequency PMN-PT-based TUTs to decrease the ultrasound attenuation and other methods for improving the penetration depth.

2.3. *PAM based on PVDF-TUTs*

Polyvinylidene fluoride (PVDF), is a flexible transparent polymer film with good piezoelectric properties, but with low electromechanical coupling efficiency ($K_t \sim 0.13$).[39] Unlike piezoelectric single crystals (LiNbO$_3$ and PMN-PT), the low acoustic impedance (~ 3.87 MRayl) and large bandwidth of PVDF allows the PVDF-TUT to require no matching layer and hold a great axial resolution.

In 2005, Niederhauser *et al.*[40] employed 200 nm thick transparent ITO electrodes instead of traditional opaque aluminum electrodes to sputter on transparent PVDF films to fabricate a TUT. Experiments show that the sensitivity of the ITO-coated PVDF is comparable to the aluminum-coated PVDF (4 mV versus 3.75 mV). Additionally, ITO's low light absorption can cause the weaker heat backward noise over the aluminum electrodes (2 mV versus 10 mV); In 2019, Pala *et al.*[41] also

produced a TUT which involves transparent PVDF, ITO, polydimethylsiloxane (PDMS) and a 3D-printed polymethil methacylate (PMMA) substrate with an inherent frequency of 300 KHz. Blumenröther *et al.*[42–44] glued PVDF to PMMA and specialized the shape of the ITO electrodes for diagnosis of the skin cancer in humans through nonfocused laser beams.

Liu *et al.*[45] proposed a PVDF-TUT with an active area of 20 mm × 20 mm for wearable PAM (Fig. 4(a)). The center frequency and −3 dB fractional bandwidth of the TUT can reach 4.75 MHz, 116.8%, respectively (Fig. 4(b)). The lateral resolution of the system is about 0.4 mm. The 3D volume imaging result of the phantom in Fig. 4(c) verifies the capability of the sensor; Fang *et al.*[46] fabricated a self-focusing TUT to increase the SNR of the received PA signals in OR-PAM. As shown in Fig. 4(d), the PVDF film is made into a concave shape and fixed onto the substrate of a planoconcave lens with an acoustic focal spot size of 0.13 mm. This type of focusing TUT combines the characteristics of both a planar TUT and a focusing ring transducer, which not only can the focused laser beams pass directly through the transducer, but also provides sound focus for the detection of PA signals. The lateral resolution of the system is 4.2 μm (Fig. 4(e)). Concurrently, the high central frequency (24 MHz) and bandwidth (26 MHz, Fig. 4(d)) of the TUT enables the greater axial resolution ($\sim 14.81\,\mu$m) and imaging quality. Although the leaf skeleton is successfully imaged (Fig. 4(e)), the sensitivity of the transducer is still limited due to the low acoustic numerical aperture (NA = 0.23) and high resistivity of ITO, which also compromises the employment of the TUT in PAM. To circumvent this problem, the group made an AR-PAM-suited PVDF-TUT[47] where the acoustic NA can reach 0.64. Contributed to the improved fabrication process, the lateral resolution can acoustically reach 37.8 μm.

2.4. *PAM based on CMUT-TUTs*

The capacitive micromachined ultrasonic transducer, which is called CMUT, is a new type of flexible ultrasonic transducers enabling to detect ultrasound signals through capacitive sensing.[48] Similar to PVDF-based TUTs, their wideband characteristics (typically tens of MHz) are very suitable for receiving broadband PA signals,
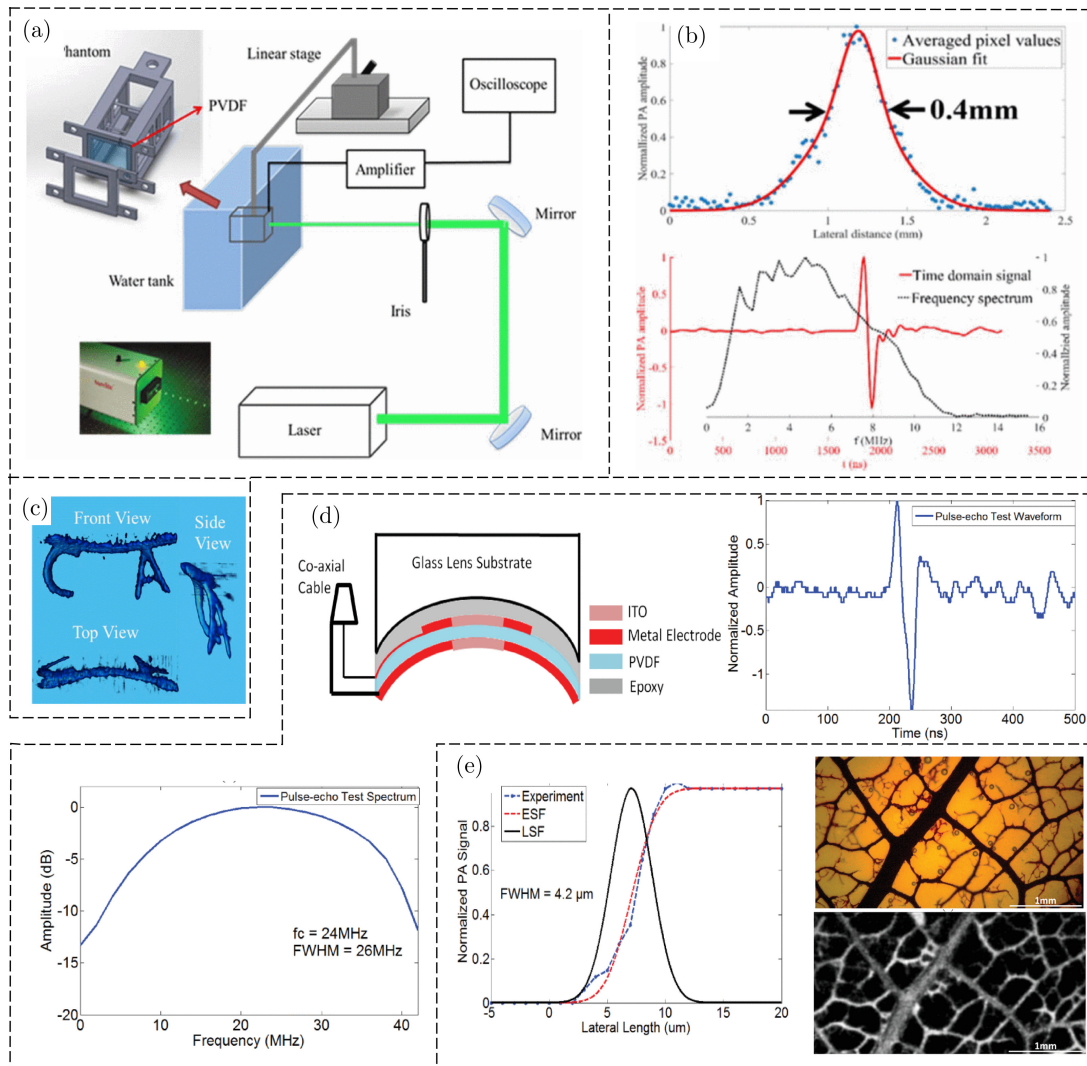
Fig. 4. (a) Imaging setup diagram of the wearable PAM system. (b) The evaluation of the lateral resolution and time-frequency response of the TUT. (c) The 3D volume imaging result of the phantom. Adapted with permission from Ref. 45. (d) Schematic design and time-frequency response of the focused PVDF-TUT. (e) Lateral resolution characterization, photograph of vein skeletons and corresponding imaging result. Adapted with permission from Ref. 46.

meanwhile, it is easy to make array integration with electronic circuits. Judging from the previous studies, nontransparent CMUTs have been successfully used for forward photoacoustic imaging (PAI).[49] The researchers are also exploring various ways to fabricate transparent CMUTs for backward PAI.

The conventional CMUTs utilize silicon as a substrate, which is opaque in the visible range but transparent in the NIR range. Based on this, Chen et al.[50] proposed a near-infrared transparent CMUT for PAI. To increase the transmittance, the thickness of the silicon substrate has been reduced to $100\,\mu m$ while the anti-reflective layer is coated to decrease the reflection rate. However, even so, the

CMUT array still has a limited transmission rate of 12% at a light wavelength of $1.06\,\mu m$. Then, Zhang et al.[51,52] used glass substrate and ITO electrodes to fabricate more transparent CMUT through the anode bonding process[53] and applied it to backward PAI (Fig. 5(B)). The CMUT mounted on a PCB has a transmittance of 40–60% with the light wavelength of 700–800 nm and a $-6\,dB$ fractional bandwidth of 105%, but the center frequency is only 1.4 MHz (Fig. 5(A)). The PA image of the indocyanine green (ICG) tube (Fig. 5(C)) suspended in agar gel to mimic biological tissue demonstrates the capability of the CMUT for PAI. Later, the group developed a 1D CMUT array[54] and corresponding
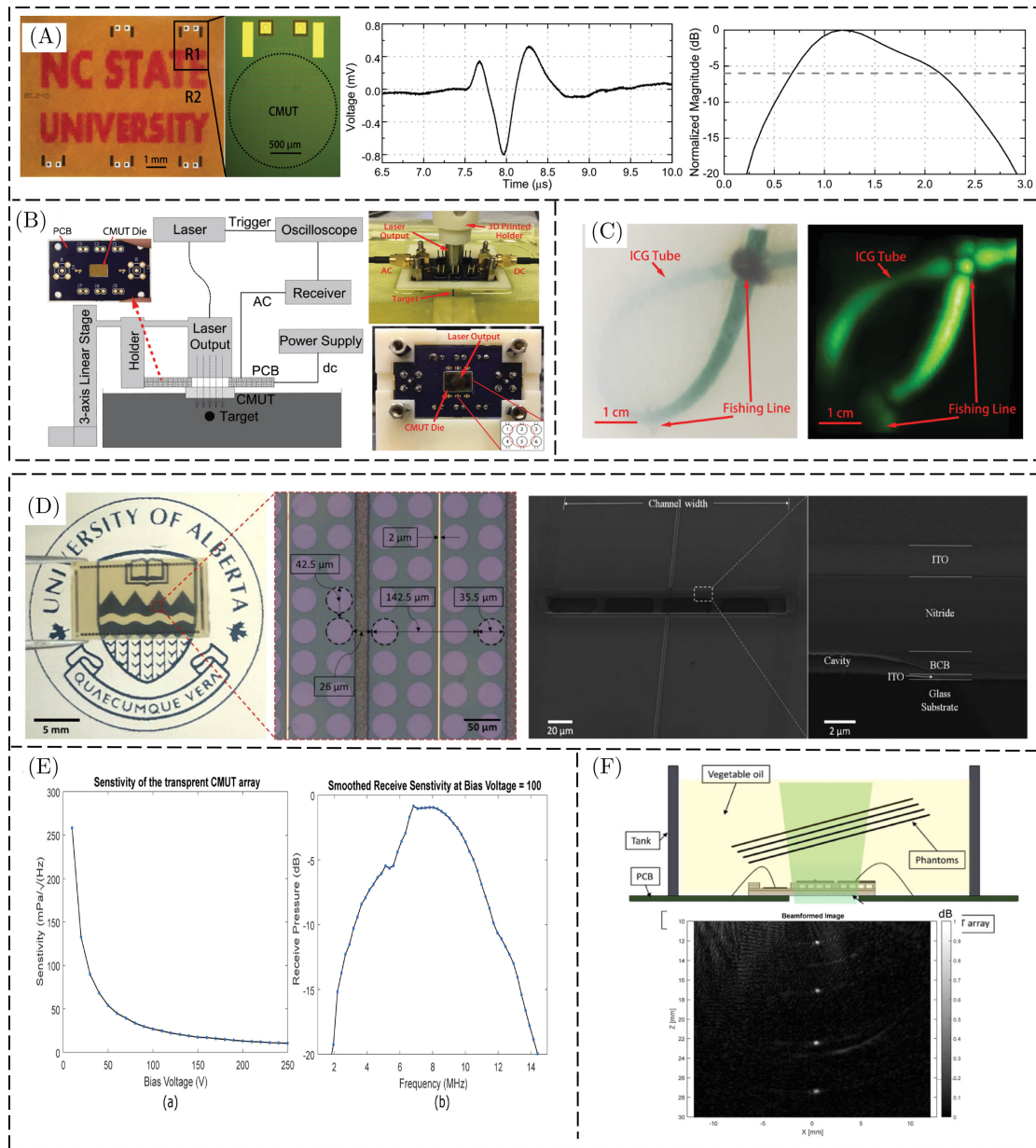
Fig. 5. (A) Optical picture of a CMUT die and time-frequency response. (B) The imaging setup diagram of the CMUT mounted on a PCB. Upper right and below right is the side view of optical fiber bundle fixed at the back of the PCB using the 3D-printed holder and bottom view of the PCB with the CMUT mounted and wire bonded on the front, respectively. Inset is relative locations of the fiber bundle output and CMUT elements. (C) The photograph of the ICG tube phantom suspended in agar gel and corresponding imaging result. Adapted with permission from Ref. 51. (D) The photo of the CMUT array, the microscope image of the die showing membranes within elements along with their associated dimensions and Helium ion microscope image of the cross-sectional structure. (E) Receive sensitivity versus bias voltage of single element of the CMUT array and frequency response. (F) Schematic view of the imaging setup and the B-scan imaging result of the gold wires phantom. Adapted with permission from Ref. 55.

electronic systems, combining the CMUT array with laser fibers and lens to create a miniaturized imaging probe.

Li *et al.*[55,56] also developed more transparent CMUTs and CMUTs array with about 70% transmittance in the visible range using silicon nitride instead of silicon as a membrane material via adhesive wafer bonding processes. To maintain the CMUTs' high optical transparency, all materials including bonding agent (BCB) and substrate (glass) are highly transparent. Figure 5(D) shows the die pitch and kerf as well as cross-sectional

structure of each channel consisting of 656 cells. The CMUT array has an operational immersion frequency of 8 MHz and a −6 dB bandwidth of 75%, respectively (Fig. 5(E)). In addition, from Fig. 5(E), we can find the received sensitivity of the CMUT is inversely proportional to the bias voltage ($10.4 \, \text{mPa}/\sqrt{\text{Hz}}$ with a bias voltage of 250 V). According to the preliminary B-scan backward PAI experiments on the 20 μm gold wire phantoms (Fig. 5(F)), the lateral and axial resolution of the system is 234 μm and 220 μm, respectively; Pang *et al.*[57] fabricated the first transparent flexible CMUT through novel roll-lamination technique other than traditional sacrificial release processes and tested the influence of several different transparent electrodes. Since ultrasonic vibrations could create cracks in other electrodes except silver nanowires, the transducer using silver nanowires as transparent electrodes is eventually fabricated.

3. Discussion and Conclusion

In PAM, the TUTs provide a path to both light delivery and acoustic detection, which has attracted more and more attention of researchers.[58] Compared with acoustic-based TUTs, despite the advantages of high sensitivity and large bandwidth, the fabrication process of the optical-based TUTs with poor mechanical stability is relatively complex. In addition, the PAM system built by the optical-TUTs uses the interference or resonance methods to detect the PA signals,[59] which requires additional expensive laser equipment. Consequently, more and more groups focus on developing acoustic-based piezoelectric TUTs because of their ease of manufacture and great compatibility with existing PAM systems involving both ultrasound excitation and sensing. In this review, some advantages of the PAM based on piezoelectric TUTs are discussed first. Then, four kinds of TUTs based on different materials and their applications in PAM are described. Different transducers have their own characteristics, and the parameters in terms of composition, size and the optical/acoustic characterization vary. Table 1 lists the different parameters of the various TUTs, from which we can see the commonalities and differences of these transducers.

As shown in Table 1, to ensure the transparency and performance of the transducer, TUTs generally use transparent epoxy or parylene as the matching/

backing and transparent ITO as the electrodes. Among these different transducers, the first three belongs to piezoelectric transducers while the last is a type of capacitive-sensing transducers based on MEMS technology. Piezoelectric TUTs feature a simple structure and inexpensive costs with the center frequency concentrating around tens of MHz. As the most frequently used TUTs in PAM, LiNbO$_3$-TUTs take advantage of the excellent light transmittance and piezoelectric performance of the active materials. They have been successfully applied to the imaging of biological tissues in *vivo*, whereas the other TUTs are limited to phantoms imaging. However, their own hard and brittle properties make it difficult to be focused to further increase the sensitivity, so adding additional acoustic lenses for focusing is helpful. The second PMN-PT-TUT is less widely used, but its performance is better than LiNbO$_3$-TUTs due to its high sensitivity and piezoelectric constant of the PMN-PT. Although the PMN-PT-TUT exhibits greater sensitivity (Table 1, Ref. 60), the optical absorption of the TUT results in limited transmittance and certain heat noise, while providing the similar imaging SNR over LiNbO$_3$-TUTs. Without imaging, currently PMN-PT-TUTs have been used to SLN A-line detection. By contrast, the PVDF-TUTs inefficiently perform in electromechanical coupling, but its large bandwidth and flexibility are still very attractive. Larger bandwidth means greater axial resolution, which is an advantage over the LiNbO$_3$-TUTs and PMN-PT-TUTs. In addition to its use in PAM, PVDF-based TUTs have also been proposed for endoscopic imaging.[61] Also, capacitive-sensing transparent CMUTs feature a good bandwidth and transparency, whereas making into an array is a development advantage. However, since CMUTs have a low central frequency ($< 20 \, \text{MHz}$), complicated manufacturing process and high costs, there are still many challenges to apply CMUTs for PAM.

Despite some advantages mentioned above, all piezoelectric and capacitive TUTs still suffer from the insufficient sensitivity, as shown in Table 1. This may be related to the high resistivity of commonly-used transparent ITO electrodes.[62] ITO has a high sheet resistance (over $100 \, \Omega/\text{sq}$), which can lead to low cut-off frequencies and loss of high frequency, decreasing the SNR of the signals. Increasing the thickness or decreasing the area of the ITO can facilitate to reduce the sheet resistance. Besides, matching and backing layers made by

Table 1. Characterization of representative TUTs.

TUTs	Ref	Composition	Size	Transparency	Performance		App
					C&BW (MHz)	S (NEP)	
LiNbO$_3$ based	31	Matching: Epoxy Electrodes: ITO Backing: None	33 mm square	73% at 512 nm	10 16.46%	none	*In vivo* mouse ear and nude mouse abdomen
	32	Matching: PC Electrodes: ITO Backing: Epoxy	10 mm diameter	80% at 450–1064 nm	37 33.9%	18 μPa/√Hz	*In vivo* mouse ear
	60	Matching: PC Electrodes: ITO Backing: Epoxy	3 mm square	90% at 532 nm	12.4 71.2%	11.9 mPa/√Hz	none
PMNPT based	37	Matching: PC + glass Electrodes: ITO Backing: None	6 mm square	73% at 532 nm	7.8 and 13.2 28.2 and 66.67%	none	Carbon fiber phantom
	38	Matching: PC+AL Electrodes: ITO Backing: Epoxy	6 mm diameter	72% at 650 nm	8 45%	none	*In vivo* SLN and melanoma detection
	60	Matching: PC Electrodes: ITO Backing: Epoxy	3 mm square	72% at 532 nm	12.4 51.6%	9.6 mPa/√Hz	none
PVDF based	45	Matching: None Electrodes: ITO Backing: None	30 × 20 mm²	none	4.75 116.8% (PA)	none	Phantoms
	46	Matching: none Electrodes: ITO Backing: epoxy	6 mm diameter	~60% at 532 nm	24 108.3%	32 μPa/√Hz	Leaf skeleton phantom
CMUT based	51	Substrate: Glass Membrane: Silicon Electrodes: ITO	none	40–60% at 600–700 nm	1.4 105%	none	ICG tube phantom
	55	Substrate: Glass Membrane: Silicon nitride Electrodes: ITO	7 × 13 mm²	70% at 600–1000 nm	8 75%	10.4 mPa/√Hz (250 V)	Golden wire phantom

Notes: Ref, reference; App, application; PC, Parylene C; AL, acoustic lens; SN, silver nanowires; PA, photoacoustic; NEP, noise equivalent pressure; C, center frequency; BW, bandwidth; S, sensitivity. SLN, sentinel lymph node.

epoxy or parylene have limited acoustic impedance (~ 3.05 Mrayl), which can also influence the sensitivity of the TUT. Therefore, choosing better matching and backing materials will help. For example, Osman *et al.*[60] proposed to use 40% volume fraction glass beads suspended in epoxy to make the translucent matching layer with the acoustic impedance reaching 4.25 MRayl, which can increase the sensitivity of the TUT by 3.3 fold. In addition, adding the transparent acoustic lens for focusing is also a good way to increase the sensitivity. Chen *et al.*[63] employed a cylindrically focused lens under the TUT to enhance the TUT's sensitivity while achieving the high-speed and wield-field scanning. Besides the drawback of the deficient sensitivity, TUTs mainly feature single element and is located at 1.4–37 MHz with narrow bandwidth, which limits

the imaging speed and 3D imaging quality to some extent. Consequently, next improvements towards the TUTs should focus on: (1) Higher sensitivity, (2) higher center frequency with wider bandwidth, and (3) multi-elements.[64]

In the field of biomedical imaging applications, currently TUTs are mainly fabricated as a round or square window for PAM. Fast and high resolution OR-PAM[65–67] is an important application branch. Benefiting from the simple structure of the TUTs, OR-PAM integrated an optically transparent window and fast scanning methods, i.e., the galvanometer and MEMS mirror, can adapt, for example, hand-held,[68] real-time wearable,[69] and large-area fast imaging occasions[70] with a cheap and light imaging head, which can contribute to monitor vasculature-associated diseases or other disorders
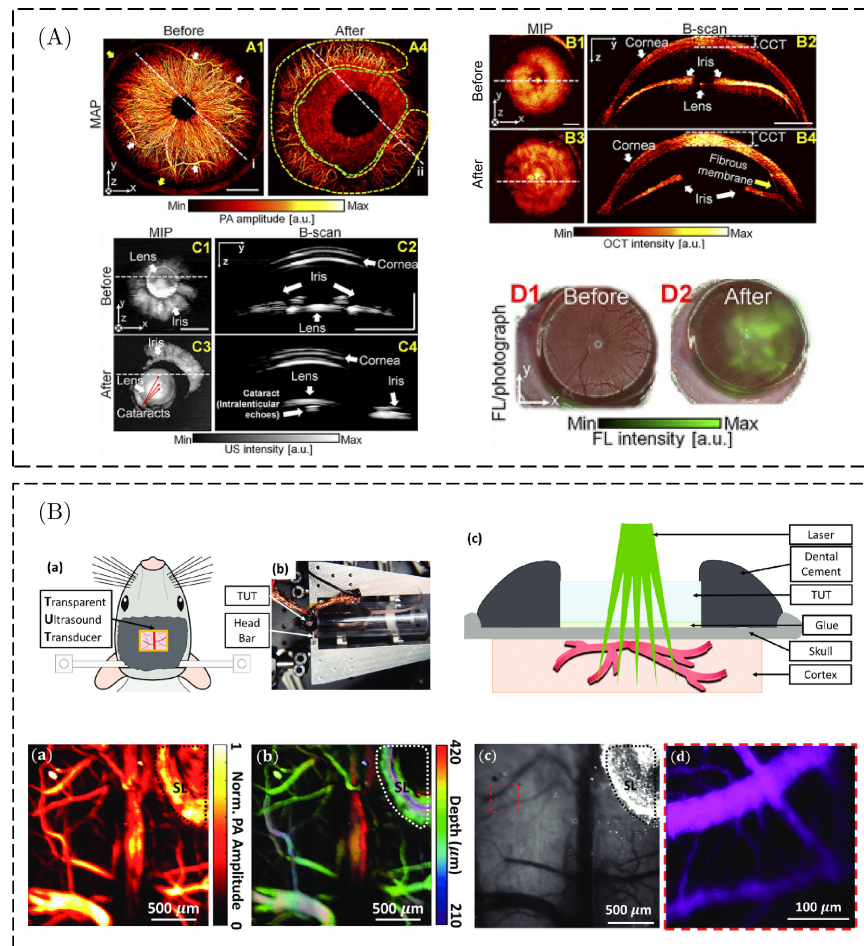

Fig. 6. (A) PA MAP images of the CNV (A1, A4), OCT MIP, corresponding B-scan image of the morphological changes and fibrous membrane (B1–B4), US MIP, corresponding B-scan image of the cataracts (C1–C4), overlaid FL and photographic image (D1, D2) of the inflammation area before and after alkali burns. Adapted with permission from Ref. 74. (B) The diagram of the transparent ultrasound cranial window and imaging results of the mouse brain were acquired by three modal imaging system through the cranial window. Adapted with permission from Ref. 75.

based on various endogenous chromophores in an early stage, such as ischemic stroke,[71] brain tumor,[72] melanoma etc. In addition, a dual-functional window for both imaging and therapy with multiple optical and acoustic based technologies is also eye-catching. From the imaging viewpoint, TUTs can naturally integrate three modalities: Optical imaging (OI), ultrasound imaging (USI), and PAI, so a multi-modal imaging platform can be realized without extra configuration. For example, Park et al.[73,74] developed a quadruple modal imaging system based on a TUT window to successfully diagnose various physiological changes caused by different disease models in rats *in vivo*. Figure 6(A) shows a series of changes recorded by the fusion imaging system in rats caused by alkali burns: Corneal neovascularization (CNV), inflammation cataracts, and newborn fibrous membranes; Chen et al.[75] reported a TUT-based mini-cranial window implanted in the head of an awake mouse for imaging of the cortical vasculature via three modes imaging technology, which provides a new way for brain imaging in rodents[76,77] (Fig. 6(B)). In comparison to the conventional optical cranial window,[78,79] the TUT combines the functions of both optical and ultrasonic sensing. With regard to another function therapy, the window allows various optical and ultrasound-based technologies to perform treatments such as photodynamic treatments (PDT) to selectively treat lesion region[80] by delivering the laser beams through the TUT or transcranial ultrasound stimulation using a focused TUT to treat depression disorder of mice. Also, we can concurrently perform both imaging and treatments based on complementary optical and ultrasound methods to achieve the purpose of integrating diagnosis with therapy.

In summary, more and more facts show that the TUT-based PAM will be an important branch of PAM development in the future. With the development of materials and technology, it is believed that these technologies will slowly move from the laboratory to the clinic and bring benefits to patients.

Acknowledgments

Conflict of Interest

There are no conflicts of interest relevant to this article.

References

1. M. W. Schellenberg, H. K. Hunt, "Hand-held optoacoustic imaging: A review," *Photoacoustics* **11**, 14–27 (2018).
2. J. Yao, L. V. Wang, "Photoacoustic microscopy," *Laser Photon. Rev.* **7**, 758–778 (2013).
3. L. Li, L. V. Wang, "Recent advances in photoacoustic tomography," *BME Front.* **2021**, 1–17 (2021).
4. C. Tian, W. Qian, X. Shao, Z. Xie, X. Cheng, S. Liu, Q. Cheng, B. Liu, X. Wang, "Plasmonic nanoparticles with quantitatively controlled bioconjugation for photoacoustic imaging of live cancer cells," *Adv. Sci.* **3**, 1600237 (2016).
5. S. Hu, L. V. Wang, "Photoacoustic imaging and characterization of the microvasculature," *J. Biomed. Opt.* **15**, 11101 (2010).
6. C. P. Favazza, O. Jassim, L. A. Cornelius, L. V. Wang, "In vivo photoacoustic microscopy of human cutaneous microvasculature and a nevus," *J. Biomed. Opt.* **16**, 16015 (2011).
7. L. J. Rich, M. Seshadri, "Photoacoustic Imaging of vascular hemodynamics: Validation with blood oxygenation level–dependent MR imaging," *Radiology* **275**, 110–118 (2014).
8. J. Laufer, P. Johnson, E. Zhang, B. Treeby, B. Cox, B. Pedley, P. Beard, "In vivo preclinical photoacoustic imaging of tumor vasculature development and therapy," *J. Biomed. Opt.* **17**, 56016 (2012).
9. E. M. Strohm, M. J. Moore, M. C. Kolios, "Single cell photoacoustic microscopy: A review," *IEEE J. Sel. Top. Quant.* **22**, 137–151 (2016).
10. Z. Xie, S. Jiao, H. F. Zhang, C. A. Puliafito, "Laser-scanning optical-resolution photoacoustic microscopy," *Opt. Lett.* **34**, 1771–1773 (2009).
11. B. Rao, K. Maslov, A. Danielli, R. Chen, K. K. Shung, Q. Zhou, L. V. Wang, "Real-time four-dimensional optical-resolution photoacoustic microscopy with Au nanoparticle-assisted subdiffraction-limit resolution," *Opt. Lett.* **36**, 1137–1139 (2011).
12. T. Jin, H. Guo, H. Jiang, B. Ke, L. Xi, "Portable optical resolution photoacoustic microscopy (pOR-PAM) for human oral imaging," *Opt. Lett.* **42**, 4434–4437 (2017).

13. J. Y. Kim, C. Lee, K. Park, G. Lim, C. Kim, "Fast optical-resolution photoacoustic microscopy using a 2-axis water-proofing MEMS scanner," *Sci. Rep.-UK* **5**, 7932 (2015).

14. Q. Chen, H. Guo, T. Jin, W. Qi, H. Xie, L. Xi, "Ultracompact high-resolution photoacoustic microscopy," *Opt. Lett.* **43**, 1615–1618 (2018).

15. K. Maslov, G. Stoica, L. V. Wang, "In vivo dark-field reflection-mode photoacoustic microscopy," *Opt. Lett.* **30**, 625–627 (2005).

16. H. Wang, X. Yang, Y. Liu, B. Jiang, Q. Luo, "Reflection-mode optical-resolution photoacoustic microscopy based on a reflective objective," *Opt. Exp.* **21**, 24210 (2013).

17. H. Estrada, J. Turner, M. Kneipp, D. Razansky, "Real-time optoacoustic brain microscopy with hybrid optical and acoustic resolution," *Laser Phys. Lett.* **11**, 45601 (2014).

18. Z. Chen, S. Yang, D. Xing, "In vivo detection of hemoglobin oxygen saturation and carboxyhemoglobin saturation with multiwavelength photoacoustic microscopy," *Opt. Lett.* **37**, 3414–3416 (2012).

19. L. Wang, K. Maslov, L. V. Wang, "Single-cell label-free photoacoustic flowoxigraphy in vivo," *Proc. Natl. Acad. Sci.* **110**, 5759–5764 (2013).

20. S. Hu, P. Yan, K. Maslov, J. Lee, L. V. Wang, "Intravital imaging of amyloid plaques in a transgenic mouse model using optical-resolution photoacoustic microscopy," *Opt. Lett.* **34**, 3899 (2009).

21. S. Hu, K. Maslov, L. V. Wang, "Second-generation optical-resolution photoacoustic microscopy with improved sensitivity and speed," *Opt. Lett.* **36**, 1134–1136 (2011).

22. J. Yao, L. Wang, C. Li, C. Zhang, L. V. Wang, "Photoimprint photoacoustic microscopy for three-dimensional label-free subdiffraction imaging," *Phys. Rev. Lett.* **112**, 14302 (2014).

23. J. Yao, L. Wang, J. Yang, K. I. Maslov, T. T. W. Wong, L. Li, C. Huang, J. Zou, L. V. Wang, "High-speed label-free functional photoacoustic microscopy of mouse brain in action," *Nat. Meth.* **12**, 407–410 (2015).

24. B. Lan, W. Liu, Y. Wang, J. Shi, Y. Li, S. Xu, H. Sheng, Q. Zhou, J. Zou, U. Hoffmann, W. Yang, J. Yao, "High-speed widefield photoacoustic microscopy of small-animal hemodynamics," *Biomed. Opt. Exp.* **9**, 4689 (2018).

25. B. Rao, L. Li, K. Maslov, L. Wang, "Hybrid-scanning optical-resolution photoacoustic microscopy for in vivo vasculature imaging," *Opt. Lett.* **35**, 1521–1523 (2010).

26. H. Li, B. Dong, X. Zhang, X. Shu, X. Chen, R. Hai, D. A. Czaplewski, H. F. Zhang, C. Sun, "Disposable ultrasound-sensing chronic cranial window by soft nanoimprinting lithography," *Nat. Commun.* **10**, 4277 (2019).

27. J. M. Cannata, T. A. Ritter, W. H. Chen, R. H. Silverman, K. K. Shung, "Design of efficient, broadband single-element (20–80 MHz) ultrasonic transducers for medical imaging applications," *IEEE Trans. Ultrason. Ferroelectr. Freq. Control.* **50**, 1548–1557 (2003).

28. G. Brodie, Y. Qiu, S. Cochran, G. C. Spalding, M. P. Macdonald, "Letters: Optically transparent piezoelectric transducer for ultrasonic particle manipulation," *IEEE Trans. Ultrason. Ferroelectr. Freq. Control* **61**, 389–391 (2014).

29. A. Dangi, S. Agrawal, S. Kothapalli, "Lithium niobate-based transparent ultrasound transducers for photoacoustic imaging," *Opt. Lett.* **44**, 5326 (2019).

30. H. Chen, S. Agrawal, A. Dangi, C. Wible, M. Osman, L. Abune, H. Jia, R. Rossi, Y. Wang, S. Kothapalli, "Optical-resolution photoacoustic microscopy using transparent ultrasound transducer," *Sensors-Basel* **19**, 5470 (2019).

31. T. Liao, Y. Liu, J. Wu, L. Zeng, X. Ji, "Centimeter-scale wide-field-of-view laser-scanning photoacoustic microscopy for subcutaneous microvasculature in vivo," *Biomed. Opt. Exp.* **12**, 2996 (2021).

32. R. Chen, Y. He, J. Shi, C. Yung, J. Hwang, L. V. Wang, Q. Zhou, "Transparent high-frequency ultrasonic transducer for photoacoustic microscopy application," *IEEE Trans. Ultrason. Ferroelectr. Freq. Control* **67**, 1848–1853 (2020).

33. H. Chen, M. Osman, S. Mirg, S. Agrawal, S. R. Kothapalli, Transparent ultrasound transducers for multiscale photoacoustic imaging, *Proc. SPIE 11642 Photons Plus Ultrasound: Imaging and Sensing 2021* (2021), p. 1164220.

34. Q. Zhou, K. H. Lam, H. Zheng, W. Qiu, K. K. Shung, "Piezoelectric single crystal ultrasonic transducers for biomedical applications," *Prog. Mater. Sci.* **66**, 87–111 (2014).

35. Y. Zhang, Z. Song, M. Lv, B. Yang, L. Wang, C. Chen, L. Feng, "Comparison of PMN–PT transparent ceramics processed by three different sintering methods," *J. Mater. Sci. Mater. Electron.* **28**, 15612–15617 (2017).

36. C. Qiu, B. Wang, N. Zhang, S. Zhang, J. Liu, D. Walker, Y. Wang, H. Tian, T. R. Shrout, Z. Xu, L. Chen, F. Li, "Transparent ferroelectric crystals with ultrahigh piezoelectricity," *Nature* **577**, 350–354 (2020).

37. H. Chen, S. Mirg, M. Osman, S. Agrawal, J. Cai, R. Biskowitz, J. Minotto, S. Kothapalli, "A high sensitivity transparent ultrasound transducer based on PMN-PT for ultrasound and photoacoustic imaging," *IEEE Sens. Lett.* **5**, 1–4 (2021).

38. B. Park, M. Han, J. Park, T. Kim, H. Ryu, Y. Seo, W. J. Kim, H. H. Kim, C. Kim, "A photoacoustic finder fully integrated with a solid-state dye laser and transparent ultrasound transducer," *Photoacoustics* **23**, 100290 (2021).

39. K. A. Snook, J. Zhao, C. H. F. Alves, J. M. Cannata, W. Chen, R. J. Meyer, T. A. Ritter, K. K. Shung, "Design, fabrication, and evaluation of high frequency, single-element transducers incorporating different materials," *IEEE Trans. Ultrason. Ferroelectr. Freq. Control* **49**, 169–176 (2002).

40. J. J. Niederhauser, M. Jaeger, M. Hejazi, H. Keppner, M. Frenz, "Transparent ITO coated PVDF transducer for optoacoustic depth profiling," *Opt. Commun.* **253**, 401–406 (2005).

41. S. Pala, L. Lin, Fully Transparent piezoelectric ultrasonic transducer with 3D printed substrate, *2019 20th Int. Conf. Solid-State Sensors, Actuators and Microsystems & Eurosensors XXXIII (TRANSDUCERS & EUROSENSORS XXXIII)*, Berlin, Germany, pp. 234–237 (2019).

42. A. Kukk, E. Blumenröther, B. Roth, "Self-made transparent optoacoustic detector for measurement of skin lesion thickness in vivo," *Biomed. Phys. Eng. Exp.* **8**, 35029 (2022).

43. E. Blumenröther, O. Melchert, J. Kanngießer, M. Wollweber, B. Roth, "Single transparent piezoelectric detector for optoacoustic sensing—Design and signal processing," *Sensors-Basel* **19**, 2195 (2019).

44. A. Varkentin, M. Mazurenka, E. Blumenröther, L. Behrendt, S. Emmert, U. Morgner, M. Meinhardt-Wollweber, M. Rahlves, B. Roth, "Trimodal system for in vivo skin cancer screening with combined optical coherence tomography-Raman and colocalized optoacoustic measurements," *J. Biophoton.* **11**, e201700288 (2018).

45. Y. H. Liu, F. S. Lin, L. X. Chen, H. Y. Su, C. H. Huang, "Wearable transparent PVDF transducer for photoacoustic imager in body sensor network," *2020 IEEE Int. Ultrasonics Symp. (IUS)*, Las Vegas, NV, USA, (2020), pp. 1–3.

46. C. Fang, H. Hu, J. Zou, "A focused optically transparent pvdf transducer for photoacoustic microscopy," *IEEE Sens. J.* **20**, 2313–2319 (2020).

47. F. Cheng, Z. Jun, "Dual-modal photoacoustic and ultrasound microscopy using optically-transparent and high-NA PVDF transducer," *Proc. SPIE.* **11960**, 1196019 (2022).

48. J. Chan, Z. Zheng, K. Bell, M. Le, P. H. Reza, J. T. W. Yeow, "Photoacoustic imaging with capacitive micromachined ultrasound transducers: Principles and developments," *Sensors-Basel* **19**, 3617 (2019).

49. A. Yasufumi, H. Yohei, S. Takahiro, N. Ken-ichi, F. Kazuhiko, S. Yoshiaki, M. Toshikazu, K. Shuichi, T. Mariko, Y. Iku, F. Elham, T. Masae, K. Masahiro, T. Masahiro, K. Shotaro, K. Masako, S. Tsuyoshi, T. Masakazu, "Photoacoustic mammography capable of simultaneously acquiring photoacoustic and ultrasound images," *J. Biomed. Opt.* **21**, 116009 (2016).

50. J. Chen, M. Wang, J. Cheng, Y. Wang, P. Li, X. Cheng, "A photoacoustic imager with light illumination through an infrared-transparent silicon CMUT array," *IEEE Trans. Ultrason. Ferroelectr. Freq. Control* **59**, 766–775 (2012).

51. X. Zhang, X. Wu, O. J. Adelegan, F. Y. Yamaner, O. Oralkan, "Backward-mode photoacoustic imaging using illumination through a CMUT with improved transparency," *IEEE Trans. Ultrason. Ferroelectr. Freq. Control* **65**, 85–94 (2018).

52. X. Zhang, O. Adelegan, F. Y. Yamaner, O. Oralkan, CMUTs on glass with ITO bottom electrodes for improved transparency, *2016 IEEE Int. Ultrasonics Symp. (IUS)*, Tours, France, pp. 1–4 (2016).

53. F. Y. Yamaner, X. Zhang, Ö. Oralkan, A three-mask process for fabricating vacuum-sealed capacitive micromachined ultrasonic transducers using anodic bonding, *IEEE Trans. Ultrason. Ferroelectr. Freq. Control* **62**, 972–982 (2015).

54. J. L. Sanders, X. Zhang, X. Wu, O. J. Adelegan, F. Y. Yamaner, M. Kudenov, Ö. Oralkan, A handheld 1D transparent CMUT array probe for photoacoustic imaging: Preliminary results, *2017 IEEE Int. Ultrason. Symp. (IUS)*, Washington, DC, USA, pp. 1–4 (2017).

55. A. K. Ilkhechi, C. Ceroici, Z. Li, R. Zemp, "Transparent capacitive micromachined ultrasonic transducer (CMUT) arrays for real-time photoacoustic applications," *Opt. Exp.* **28**, 13750 (2020).

56. Z. Li, A. K. Ilkhechi, R. Zemp, "Transparent capacitive micromachined ultrasonic transducers (CMUTs) for photoacoustic applications," *Opt. Exp.* **27**, 13204 (2019).

57. D. Pang, C. Chang, "Development of a novel transparent flexible capacitive micromachined ultrasonic transducer," *Sensors-Basel* **17**, 1443 (2017).

58. D. Ren, Y. Sun, J. Shi, R. Chen, "A review of transparent sensors for photoacoustic imaging applications," *Photonics* **8**, 324 (2021).

59. B. Dong, C. Sun, H. F. Zhang, "Optical detection of ultrasound in photoacoustic imaging," *IEEE T. Bio.-Med. Eng.* **64**, 4–15 (2017).

60. S. Mirg, H. Chen, S. Khandare, M. Osman, S. Kothapalli, "Noise considerations in piezoelectric transparent ultrasound transducers for photoacoustic imaging applications," *Proc. SPIE.* **11960**, 119600S (2022).

61. T. Zhao, S. Ourselin, T. Vercauteren, W. Xia, "Miniaturized transparent ultrasound sensor for

photoacoustic endoscopy," *Proc. SPIE.* **11960**, 1196009 (2022).

62. M. Mazur, D. Kaczmarek, J. Domaradzki, D. Wojcieszak, S. Song, F. Placido, Influence of thickness on transparency and sheet resistance of ITO thin films, *Eighth Int. Conf. Advanced Semiconductor Devices and Microsystems*, 25–27 October, 2010, Smolenice, Slovenia, pp. 65–68.

63. M. Chen, L. Jiang, C. Cook, Y. Zeng, T. Vu, R. Chen, G. Lu, W. Yang, U. Hoffmann, Q. Zhou, J. Yao, "High-speed wide-field photoacoustic microscopy using a cylindrically focused transparent high-frequency ultrasound transducer," *Photoacoustics* **28**, 100417 (2022).

64. H. Chen, S. Agrawal, M. Osman, J. Minotto, S. Mirg, J. Liu, A. Dangi, Q. Tran, T. Jackson, S. Kothapalli, "A transparent ultrasound array for real-time optical, ultrasound, and photoacoustic imaging," *BME Front.* **2022**, 9871098 (2022).

65. J. Park, B. Park, T. Y. Kim, S. Jung, W. J. Choi, J. Ahn, D. H. Yoon, J. Kim, S. Jeon, D. Lee, U. Yong, J. Jang, W. J. Kim, H. K. Kim, U. Jeong, H. H. Kim, C. Kim, "Quadruple ultrasound, photoacoustic, optical coherence, and fluorescence fusion imaging with a transparent ultrasound transducer," *Proc. Natl. Acad. Sci.* **118**, e1920879118 (2021).

66. S. Mirg, H. Chen, K. L. Turner, K. W. Gheres, J. Liu, B. J. Gluckman, P. J. Drew, S. R. Kothapalli, "Awake mouse brain photoacoustic and optical imaging through a transparent ultrasound cranial window," *Opt. Lett.* **47**, 1121–1124 (2022).

67. C. T. Sullender, A. E. Mark, T. A. Clark, T. V. Esipova, S. A. Vinogradov, T. A. Jones, A. K. Dunn, "Imaging of cortical oxygen tension and blood flow following targeted photothrombotic stroke," *Neurophotonics* **5**, 1 (2018).

68. J. Senarathna, H. Yu, C. Deng, A. L. Zou, J. B. Issa, D. H. Hadjiabadi, S. Gil, Q. Wang, B. M. Tyler, N. V. Thakor, A. P. Pathak, "A miniature multi-contrast microscope for functional imaging in freely behaving animals," *Nat. Commun.* **10**, 99 (2019).

69. İ. Şencan, T. Esipova, K. Kılıç, B. Li, M. Desjardins, M. A. Yaseen, H. Wang, J. E. Porter, S. Kura, B. Fu, T. W. Secomb, D. A. Boas, S. A. Vinogradov, A. Devor, S. Sakadžić, "Optical measurement of microvascular oxygenation and blood flow responses in awake mouse cortex during functional activation," *J. Cereb. Blood Flow Metab.* **42**, 510–525 (2022).

70. S. Jeon, J. Kim, D. Lee, J. W. Baik, C. Kim, "Review on practical photoacoustic microscopy," *Photoacoustics* **15**, 100141 (2019).

71. Q. Chen, H. Xie, L. Xi, "Wearable optical resolution photoacoustic microscopy," *J. Biophoton.* **12**, e201900066 (2019).

72. P. Wray, L. Lin, P. Hu, L. V. Wang, "Photoacoustic computed tomography of human extremities," *J. Biomed. Opt.* **24**, 1 (2019).

73. J. Lv, S. Li, J. Zhang, F. Duan, Z. Wu, R. Chen, M. Chen, S. Huang, H. Ma, L. Nie, "In vivo photoacoustic imaging dynamically monitors the structural and functional changes of ischemic stroke at a very early stage," *Theranostics* **10**, 816–828 (2020).

74. X. Gong, T. Jin, Y. Wang, R. Zhang, W. Qi, L. Xi, "Photoacoustic microscopy visualizes glioma-induced disruptions of cortical microvascular structure and function," *J. Neural Eng.* **19**, 26027 (2022).

75. S. Park, S. Kang, J. H. Chang, "Optically transparent focused transducers for combined photoacoustic and ultrasound microscopy," *J. Med. Biol. Eng.* **40**, 707–718 (2020).

76. S. Bodea, G. G. Westmeyer, "Photoacoustic neuroimaging — Perspectives on a maturing imaging technique and its applications in neuroscience," *Front. Neurosci.* **15**, 655247 (2021).

77. X. Wang, Y. Luo, Y. Chen, C. Chen, L. Yin, T. Yu, W. He, C. Ma, "A skull-removed chronic cranial window for ultrasound and photoacoustic imaging of the rodent brain," *Front. Neurosci.* **15**, 673740 (2021).

78. M. Alieva, L. Ritsma, R. J. Giedt, R. Weissleder, J. van Rheenen, "Imaging windows for long-term intravital imaging," *IntraVital* **3**, e29917 (2014).

79. A. Holtmaat, T. Bonhoeffer, D. K. Chow, J. Chuckowree, V. De Paola, S. B. Hofer, M. Hübener, T. Keck, G. Knott, W. A. Lee, R. Mostany, T. D. Mrsic-Flogel, E. Nedivi, C. Portera-Cailliau, K. Svoboda, J. T. Trachtenberg, L. Wilbrecht, "Long-term, high-resolution imaging in the mouse neocortex through a chronic cranial window," *Nat. Protoc.* **4**, 1128–1144 (2009).

80. D. E. J. G. Dolmans, D. Fukumura, R. K. Jain, "Photodynamic therapy for cancer," *Nat. Rev. Cancer* **3**, 380–387 (2003).